Three times accelerated glacier area loss in Svalbard revealed by deep learning

Konstantin A. Maslov[1,*], Thomas Schellenberger[2], Claudio Persello[1], Alfred Stein[1]

[1] Department of Earth Observation Science, Faculty of Geo-information Science and Earth Observation (ITC), University of Twente, Drienerlolaan 5, 7522NB Enschede, Overijssel, The Netherlands
[2] Department of Geosciences, Faculty of Mathematics and Natural Sciences, University of Oslo, Sem Sælands vei 1, Blindern, 0371 Oslo, Østlandet, Norway
[*] email: k.a.maslov@utwente.nl.

Abstract

The rapid warming in polar regions highlights the need to monitor climate change impacts such as glacier retreat and related global sea level rise. Glacier area is an essential climate variable but its tracking is complicated by the labour-intensive manual digitisation of satellite imagery. Here we introduce ICEmapper, a deep learning model that maps glacier outlines from Sentinel-1 time series with accuracy on par with human experts. We used this model to retrieve Svalbard glacier outlines for 2016–2024 and found a tripling of the glacier area loss rate ($-260\,\mathrm{km}^2\,\mathrm{a}^{-1}$) in the last decade as compared to that previously reported for 1980–2010 ($-80\,\mathrm{km}^2\,\mathrm{a}^{-1}$). This acceleration is largely driven by increased calving at tidewater glaciers and the climatic warming signal impacting land-terminating glaciers. Additionally, our analysis shows significant area changes related to glacier surging, namely, the Nathorstbreen system and Austfonna, Basin-3 surges. These two surges collectively added to the area change in 2006–2016 ($+194.30\,\mathrm{km}^2$ or $+0.59\%$), thus delaying the regionwide area loss by approximately two years. Our results indicate a significant acceleration in glacier area loss in Svalbard, and we anticipate broader applications of our method to track glacier changes on larger scales.

Introduction

Glaciers serve as crucial indicators of climate change, providing valuable insights into environmental shifts due to the sensitivity to temperature and precipitation changes [1–5]. The Arctic region is experiencing rapid warming known as Arctic amplification, where temperatures are rising nearly four times faster than the global average [6]. This accelerated warming is particularly evident in regions like Svalbard [7], an Arctic archipelago where glaciers cover approximately 57% of the land area [8]. The rapid changes observed in Svalbard glaciers make it a critical zone for understanding climate processes and their impacts on polar environments [9–12].

The Global Climate Observing System (GCOS) recognises "glacier area" as one of the essential climate variables, but the recommended decadal-scale monitoring standards are rarely met [13]. In addition, traditional glacier monitoring methods, relying on optical satellite imagery, often suffer from limited temporal resolution due to cloud cover at the end of the ablation season when landscapes are free of seasonal snow [14]. In Svalbard, a glacier area loss rate of $\approx -80\,\mathrm{km}^2\,\mathrm{a}^{-1}$ was reported for 1980–2010 [8]. In the last decade, the only two inventories available are from 2016/2017 [15] and 2020 [16] with remarkable differences in the principles used to outline glaciers. These observational gaps and inconsistencies make tracking the changing glacier area in a timely and accurate manner challenging.

Synthetic Aperture Radar (SAR) technology, particularly through the Sentinel-1 mission, has the potential to greatly improve our ability to generate regular glacier inventories by offering consistent and high-temporal-resolution data regardless of weather conditions or daylight availability. This enhanced temporal resolution is particularly valuable for constraining physical models of glacier evolution, especially when studying rapidly changing phenomena such as calving fronts [17] and glacial surges, thus, leading to new insights into glacier dynamics.

Interferometric SAR (InSAR) coherence is generally recognised as a strong predictor for glacier outlines, especially for debris-covered tongues [18, 19]. Furthermore, SAR backscatter drops significantly during the melting season due to increased absorption of the radar signal by liquid water and reduced volumetric scaterring [20]. This temporal signal has been widely adopted to identify and monitor glacier surface types [21, 22]. Despite its potential, the applicability of SAR time series to automate glacier outlines mapping remains largely underexplored.

In this study, we introduce Intensity-Coherence-Evolution-mapper (ICEmapper), a deep learning model designed to map glacier outlines annually from Sentinel-1 time series in Svalbard. We systematically quantify uncertainties for both pixel-level predictions and overall area estimates—an aspect that has rarely been addressed comprehensively in deep-learning-based remote sensing and in previous glacier mapping efforts. We train ICEmapper using the 2016/2017 [15] and 2020 [16] glacier inventories. We apply this model to derive annual glacier outlines for the period 2016–2024 across Svalbard and analyse the glacier area changes. Our results show the increased response of glacier area to climate change in Svalbard and demonstrate the potential of our approach for tracking glacier changes, offering new perspectives on the dynamics of glacial ice loss.

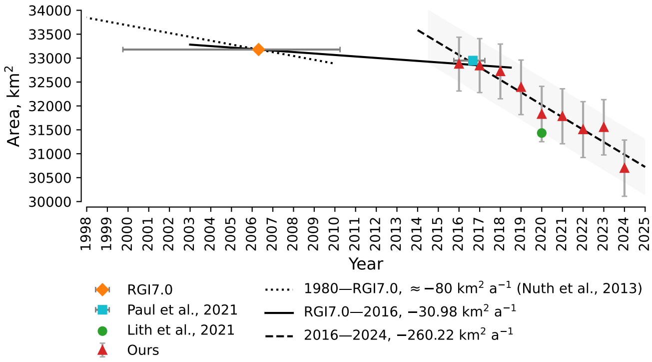

Fig. 1 Total glacier area change in Svalbard, except Kvitøya. X-error bands indicate minimum and maximum years for inventories derived from multi-year imagery, and y-error bands stand for the 95%-confidence interval for the total area (see Methods for details).

Results

Glacier area change analysis. To contextualise the results, we defined two distinct epochs of area change: (1) RGI7.0–2016 compares the Randolph Glacier Inventory 7.0 (RGI7.0) outlines [23] with our 2016 inventory, and (2) 2016–2024 analyses the annual inventories derived from ICEmapper. As RGI7.0 is a multi-year inventory with outlines obtained in the period from 2000 to 2010, we assumed the effective year of RGI7.0 to be its area-weighted average year (≈ 2006). Figure 1 shows the total glacier area evolution over the whole of Svalbard except Kvitøya, an island in the northeast part of the archipelago.

In the RGI7.0–2016 epoch, the glacier area declined by $-300.11\,\mathrm{km}^2$ in total at a rate of $-31 \pm 59\,\mathrm{km}^2\,\mathrm{a}^{-1}$. Notably, two large surges—–the Nathorstbreen system ($+107.76\,\mathrm{km}^2$) started in 2009 [24] and Austfonna, Basin-3 ($+86.54\,\mathrm{km}^2$) in 2012 [25]—–temporarily offset these losses. Their combined effect ($+194.30\,\mathrm{km}^2$ or $+0.59\%$) is estimated to have delayed net area shrinkage by around two years during the RGI7.0–2016 epoch. Subtracting the significant area gains of the advances of Nathorstbreen and Basin-3 from the trend of the RGI7.0–2016 epoch shows a more representative regionwide trend of $-51.03\,\mathrm{km}^2\,\mathrm{a}^{-1}$. Other parts of the archipelago show both positive (e.g., the northern part of Austfonna and the northeast of Spitsbergen) and negative (Edgeøya and the northwest of Spitsbergen) glacier area change trends (Figure 2a).

The annual inventories from ICEmapper between 2016–2024 reveal a sharply accelerated loss of glacier area of $-2081.74\,\mathrm{km}^2$ at a rate of $-260 \pm 75\,\mathrm{km}^2\,\mathrm{a}^{-1}$ (or $-0.79 \pm 0.23\%\,\mathrm{a}^{-1}$) throughout the archipelago. The net retreat is widespread (Figure 2b), with one considerable positive anomaly observed in Austfonna, Basin-7. This localised area increase stems from a previously unreported surge event initiated around 2018/2019 (see Supplementary Notes).

We separately mapped Kvitøya using optical satellite imagery and GlaViTU [27], an existing glacier mapping model. The island was not included in the SAR-based inventories due to its coverage by a different radar imaging mode with a lower spatial resolution (see the Methods section for more detail). The glacier area change trend of Kvitøya from 2016 to 2024 is $-2.58\,\mathrm{km}^2\,\mathrm{a}^{-1}$ (or $-0.42\%\,\mathrm{a}^{-1}$), notably lower than the relative archipelago-wide rate reported above likely due to its location further north, yet still indicating a persistently negative trend.

Differentiating between tidewater and land-terminating glaciers reveals mixed results in the RGI7.0–2016 epoch: while their mean area change rates do not differ significantly (p-value > 0.05; compared using a two-sided Welch's t-test), the median rates do (p-value < 0.05; compared using a two-sided Mann-Whitney U test; Figure 3a). The same tests were used for comparing means and medians throughout this manuscript. In contrast, the 2016–2024 epoch exhibits statistically significant distinctions in both means and medians, with tidewater glaciers undergoing a more pronounced retreat on average (Figure 3b). Both tidewater and land-terminating glaciers show statistically significant acceleration in their area loss (p-value < 0.05) when comparing RGI7.0–2016 to 2016–2024. In total, tidewater glaciers contributed $-240.57\,\mathrm{km}^2$ (or 80.16%) to the overall glacier area loss in the RGI7.0–2016 epoch. By contrast, tidewater glaciers accounted for $-688.43\,\mathrm{km}^2$ (33.07%) of area loss in the 2016–2024 epoch.

For land-terminating glaciers in the RGI7.0–2016 epoch, there is a modest but statistically significant correlation ($r_s = 0.32$, p-value < 0.05; Supplementary Figure 2) between area change rates and climatic mass-balance values modelled for the same period [28]. In the case of tidewater glaciers, no significant correlation was identified ($r_s = 0.13$, p-value > 0.05; Supplementary Figure 2), suggesting that processes at the ice-ocean interface play a dominant role in determining frontal ablation rates.

No significant difference in area change trends emerges between known surging [26] and non-surging glaciers in the RGI7.0–2016 epoch (p-value > 0.05; Figure 3c). In the 2016–2024 epoch, however, the area loss rates among surging glaciers are significantly higher (p-value < 0.05 for both means and medians; Figure 3d) compared to their non-surging counterparts, implying more rapid retreat on average. These conclusions remain the same in both epochs when restricting the analysis to surging tidewater glaciers alone. This contrast is apparent even though individual surges can cause short-term area gains.

ICEmapper performance. Given the ten-year analysis span and the comparably limited area change observed, it is crucial to ensure that our model meets accuracy requirements. The derived glacier outlines exhibit

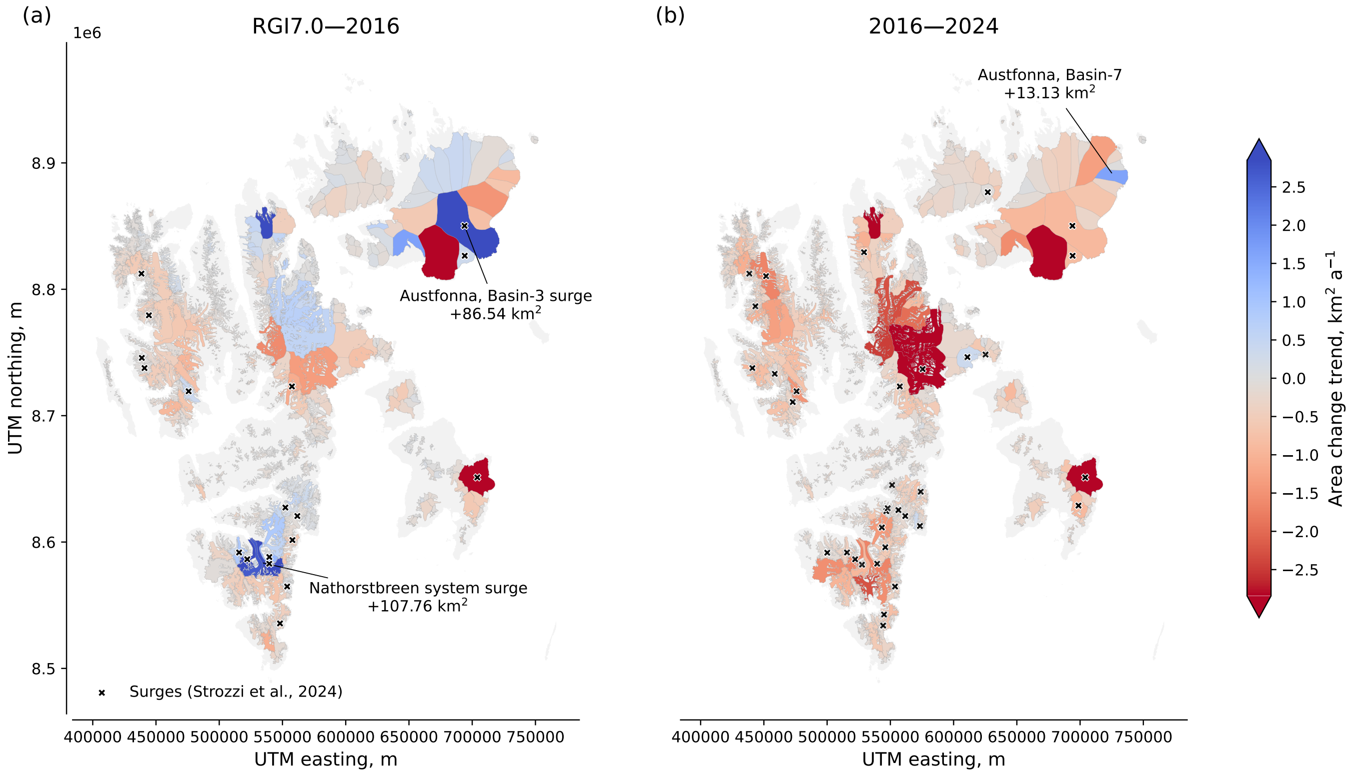

Fig. 2 Glacier area change trend maps: a for the RGI7.0–2016 epoch and **b** for the 2016–2024 epoch. The glacier outlines and ice divides are taken from Kohler et al., 2021 [16], and the glacier surge inventory is from Strozzi et al., 2024 [26].

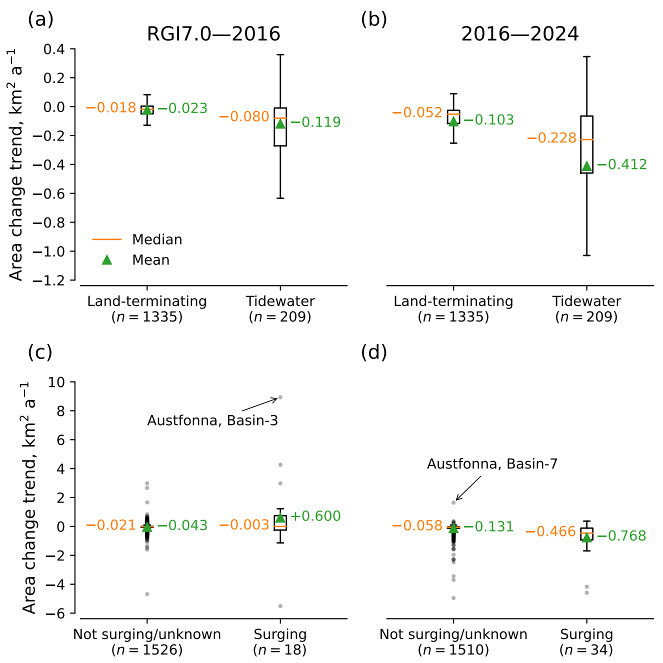

Fig. 3 Comparison of glacier area change trends: a, b for land-terminating vs tidewater and **c, d** for not surging vs surging glaciers **a, c** in the RGI7.0–2016 epoch and **b, d** in the 2016–2024 epoch.

accuracy equivalent to human experts when delineating glaciers from optical images [29–31], with intersection over union (IoU) score higher than 0.95, total area discrepancies below 0.5%, a median distance deviation of approximately 15 m (or 1.5 pixel) and the 95$^{\text{th}}$ percentile distance deviation under 250 m (Table 1), affirming its effectiveness for glacier monitoring. Qualitative assessments also show good correspondence between the reference inventories and the modelled outlines, however, the performance over small glaciers and tributary tongues remains inconsistent (Supplementary Figure 4). On the other hand, we like to highlight the IoU of 0.992, an almost 100% match between the reference and model outlines for the 2016 test subset covering two ice caps—Austfonna and Vestfonna (Table 1).

Calibration of the modelled confidence against the actual accuracy yielded reliable per-pixel confidence estimates with expected calibration error below 0.5%, highlighting the areas prone to classification errors (Supplementary Figure 4). In particular, the pixel-level confidence maps allow confident detection of significant terminus shifts over the years, supporting spatio-temporal analyses of glacier front evolution (Supplementary Figure 5).

Discussion

Overall, our annual glacier inventories for Svalbard reveal a substantial acceleration of area loss since 2016. Comparisons against earlier estimates highlight a markedly faster rate of glacier recession, approximately $-260\,\mathrm{km}^2\,\mathrm{a}^{-1}$ (or $-0.79\%\,\mathrm{a}^{-1}$) in 2016–2024, which is more than three times the reported $-80\,\mathrm{km}^2\,\mathrm{a}^{-1}$ from 1980–2010 [8]. Extending the perspective further back to an existing 1936/1938 inventory [32] implies that overall retreat now proceeds at rates five to six times higher than the area change trend of approximately $-44\,\mathrm{km}^2\,\mathrm{a}^{-1}$ observed in the 1936/1938–RGI7.0 period, at least in the regions consistently covered in both the 1936/1938 inventory and RGI7.0, which are the whole of the archipelago except Kvitøya and some Eastern parts of Austfonna. These historical comparisons, however, rely on temporally sparse data sources that lack consistent spatial coverage and uncertainty quantification, making the trend estimation somewhat uncertain. By contrast, the annual inventories presented here provide direct estimates of uncertainty at both pixel and archipelago scales, which enable a more robust assessment of modern glacier changes. Notably, our results suggest the largest annual glacier area loss in 2024, which was the warmest year on record both regionally and globally, although the attribution to this climatic extreme is partly obscured by the model uncertainty.

Looking to the future, negative mass balance projections for Svalbard[33] suggest that the glacier area will continue to decline. Even a halt in warming would not prevent further area loss due to the temporal lag between the climatic forcing and glacier geometry response [34] as most glaciers remain out of equilibrium with present climatic conditions. For tidewater glaciers in particular, declining seasonal sea ice duration [35] is likely to further exacerbate retreat as the presence of sea ice helps stabilise calving fronts [36–38]. Increased ocean heat content is expected to accelerate the area loss of tidewater glaciers as well [39].

Although both land-terminating and tidewater glacier types exhibit accelerating shrinkage, the 2016–2024 data indicate substantially higher retreat rates among tidewater glaciers, which are more sensitive to oceanic influences such as submarine melt and calving [39, 40]. In parallel, land-terminating glaciers display a measurable correlation with climatic mass balance, implying a primary driver related to atmospheric warming and, thus, surface melt. While the precise weighting of these processes remains an active research topic, the general message is that multiple climate forcings—–both atmospheric and oceanic—–contribute to the overall glacier recession ongoing in Svalbard. In total, while tidewater glaciers remain an important driver of the negative glacier area trend, land-terminating glaciers comprise a larger fraction of the most recent, and higher, overall area loss.

Turning to surging glaciers, large individual events can mask the underlying regional trend by imparting glacier area gains, thereby introducing non-linearity into the overall time series, as exemplified by Nathorsbreen and Austfonna, Basin-3. The analysis also shows that the average area change rates of the surging glaciers in 2016–2024 exceed those of non-surging glaciers. A plausible interpretation is that large individual surges, although adding glacier area temporarily, lead to a more pronounced retreat after the active surge phase ends, linked to thinning-induced dynamic instabilities and higher incidence of calving [25] due to, e.g., increased crevassing [41] and lateral wastage [8]. Moreover, the mass redistribution during surges typically lowers the elevation in the accumulation zone by tens of meters as well as effectively transport ice to the terminus area [37, 42], exposing both to warmer air and, thus, intensifying melt [43]. Further monitoring over extended periods is necessary to confirm whether the higher losses among surging glaciers reflect a consistent trend or whether it is partly coincidental within our relatively short observation window of a decade.

Additionally, we recognized an increasingly larger extent and surge-induced glacier area encroachment from adjacent flow units at the kilometre scale, while tracking the low coherence zone of, e.g., Austfonna, Basin-3 (Supplementary Figure 10). Because our inventories rely on static ice divides copied from the existing datasets, these surge-driven changes are not fully captured, highlighting the need for more frequent ice divide updates derived from velocity products that can better resolve glacier flow boundaries. Such refined delineations would also benefit ice cap-wide glacier evolution modelling.

While the overall accuracy of ICEmapper aligns closely with expert digitisation and demonstrates robust performance on most glacier margins, the model exhibits inconsistencies in mapping smaller ice masses and tributaries. These localised errors are likely driven by a combination of limited feature contrast of glaciers in SAR imagery and variations in how small glaciers were delineated across different reference inventories used for training, as the 2016/2017 inventory [15] tends to include smaller ice patches in general. Future work should test the transferability of ICEmapper to regions with higher debris cover and steeper terrain, as well as to other SAR platforms with longer revisit times and irregular acquisition schedules. Moreover, improvements could include utilising images from both ascending and descending passes, higher-resolution SAR data, more sophisticated data fusion methods that incorporate, e.g., optical or thermal imagery and the expansion of training sets to cover a broader diversity of glacier types and environmental conditions. Such expansions would facilitate a more globally consistent framework for glacier mapping and enable future applications of ICEmapper to other polar and high-mountain regions experiencing glacier retreat, fulfilling the GCOS standards for glacier area monitoring.

In summary, our annual glacier outlines indicate that Svalbard has entered a phase of accelerated glacier area loss in the last years, likely driven by the combined influences of warming atmospheric and ocean conditions. Despite certain limitations, such as reduced accuracy for smaller ice patches, the results demonstrate the utility of an automated deep learning method for generating high-temporal-resolution (i.e., annual) glacier inventories, enabling regionwide glacier area change analysis at decadal or shorter time scales. Continued monitoring in Svalbard and other regions at annual intervals will be essential to better understand processes that govern glacier recession, inform glacier evolution models and evaluate the impacts of cryospheric changes on sea-level contributions and polar environments.

Methods

Study area and data. Our study focused on Svalbard, utilising Sentinel-1A imagery to cover almost the entirety of the region, excluding Kvitøya. The satellite data included images from two ascending orbit stripes (relative orbits 14 and 174) acquired in the interferometric wide (IW) swath mode. To train our models, we used 30 co-polarized (HH) ground range detected (GRD) and radiometrically terrain corrected (RTC) [44]

Table 1 Test performance of ICEmapper. The reported metrics are defined in Methods, Accuracy Assessment.

Year	Number of test tiles	Pixel-wise IoU	Precision	Recall	Distance deviation, m			Total area deviation	
					Mean	Median	95^{th} percentile	km^2	%
2016	34	0.992	0.996	0.996	34.17	0	118.75	+0.47	+0.02
2017	143	0.951	0.977	0.972	57.35	15.53	202.83	−25.33	−0.46
2020	179	0.965	0.982	0.982	63.28	14.42	207.78	+0.47	+0.01
Total	356	0.964	0.982	0.981	58.68	13.41	198.12	−24.39	−0.16

mosaics per year. These images were resampled to a spatial resolution of $10\,\text{m} \times 10\,\text{m}$ from the original resolution of $5\,\text{m} \times 20\,\text{m}$, with a 12-day interval between acquisitions. Additionally, we incorporated InSAR coherence imagery into our analysis computed at the 12-day temporal baseline. For reference data in training and evaluation, we utilised two glacier inventories from the years 2016/2017 [15] and 2020 [16] (a preliminary version, kindly provided by the authors). The 2016/2017 inventory was spatially and temporally uncoupled, meaning that images from 2016 and 2017 were used distinctly according to their corresponding outlines. The whole geographical domain was divided into 734 square tiles, each measuring 10 km by 10 km. We randomly allocated 60% of the tiles to use for training, 20% for validation, and the remaining 20% for testing. Tiles that did not cover glacierised landmass were excluded from the training dataset, as well as Kvitøya island due to its coverage by Sentinel-1 in a different imaging mode with a lower spatial resolution as compared to the rest of the archipelago. For generating the final glacier inventories, we utilised 15 scenes per year with a 24-day gap between acquisitions. The temporal baselines for the InSAR coherence images were maintained at 12 days for all years, except 2024 where the 24-day baseline provided qualitatively better outcomes. An overview of the study area is provided in Supplementary Figure 3.

ICEmapper. We refined our previous glacier mapping method [45] by introducing a revised model called Intensity-Coherence-Evolution-mapper (ICEmapper, Supplementary Figure 6), which transforms a one-year time series of SAR images into glacier outlines as they are observed at the end of the ablation season. ICEmapper is based on the U-Net architecture [46] and incorporates 3D convolutions in the decoder part to process temporal and spatial dimensions simultaneously similar to other studies [47].

Patches of 384×384 pixels were extracted randomly for model training. From the 30 available timesteps per year, 15 were sampled for training, each spaced by a 24-day gap. To further enhance the robustness to temporal variations, we introduced random noise of ± 12 days for individual timesteps to the sampling as part of the data augmentation process. Additionally, data augmentation included random flipping, rotation, cropping, rescaling, contrast γ-transformation and Gaussian noise introduction. The optimisation was performed using Adam [48] minimising focal loss [49] with the addition of label smoothing [50]. We employed a cosine annealing schedule with warm restarts for the learning rate [51], initiating at $5e^{-4}$ and progressing through four training phases of 10, 20, 40, and 80 epochs. Selection for further evaluation was restricted to models demonstrating the highest performance on the validation subset.

Compared to our previous study [45], we replaced the max pooling layers with time-weighted pooling (Supplementary Figure 7) to allow for more adaptive extraction of the temporal features. The time-weighted pooling effectively computes a weighted average of the hidden representations along the temporal dimension, where the weights are calculated from the data itself. The time-weighted pooling showed marginal validation performance gains (Supplementary Table 1) and demonstrated better convergence properties (Supplementary Figure 8), hence, we used the time-weighted pooling layers in the rest of the experiments.

We additionally explored various feature sets including GRD, RTC and InSAR coherence data, as well as combinations of GRD and RTC with InSAR. Our results indicate that the combination of GRD and InSAR achieves the best overall validation performance (Supplementary Table 1), though the performance gap from RTC and InSAR was rather minor. Given the additional processing step for the generation of RTC imagery, the GRD and InSAR combination provides a more computationally efficient alternative as well. We, thus, used GRD and InSAR to report the test performance and produce the final glacier inventories. The test performance of ICEmapper aligns with the expertise level of human analysts [29–31] with the total area difference $< 0.5\%$, median distance deviation $\approx 15\,\text{m}$ and the 95^{th} distance deviation percentile $< 250\,\text{m}$ (Table 1).

Postprocessing. We implemented several procedures to eliminate some spurious predictions. We removed all polygons smaller than $0.01\,\text{km}^2$ following a common practice in glacier inventory generation [52]. We also excluded any positive predictions that extended beyond the boundaries of a 3840 m buffer, which was established based on the union of known glacier inventories including RGI7.0 [23] and the inventories used in this study [15, 16]. This buffer served as a spatial constraint to refine our analysis to areas with confirmed glacier presence.

An additional temporal filtering was applied to the pixel-level predictions. If a pixel was classified as a glacier in a given year t_i but was predicted with high confidence ($> 90\%$) as non-glacier in adjacent years t_{i-1} and t_{i+1}, the classification for the year t_i was revised to non-glacier. This correction was also applied in reverse—if a pixel was classified as non-glacier at t_i yet identified as glacier with high confidence in t_{i-1} and t_{i+1}, it was reclassified as glacier for the year t_i.

As the pixel-level temporal filtering cannot be applied to years 2016 and 2024, as a similar measure we removed all isolated polygons $> 1\,\text{km}^2$ that do not have intersections with any polygon from the adjacent years in the predictions, assuming that large ice complexes do not appear and disappear suddenly. These measures ensured overall higher temporal consistency of the generated inventories.

Uncertainty quantification. We used plain softmax scores from a single forward pass to assess classification confidence, similar to our other work [27]. We employed a Shannon-entropy-based metric to measure confidence:

$$\text{conf}\,(S_i) = 1 + (1 - S_i)\,\log_2 (1 - S_i) + S_i \log_2 S_i\,, \qquad (1)$$

where S_i is the softmax score attributed to the glacier class at the i^{th} pixel, and $\log_2(\,\cdot\,)$ denotes the logarithm base 2. Initially, these scores exhibited high underconfidence. To enhance the reliability of our uncertainty estimates, we implemented a confidence calibration approach through kernel ridge regression aimed at aligning the predicted confidence levels with actual model accuracy. This calibration significantly reduced the expected calibration error to $< 0.5\%$ (Supplementary Figure 9) allowing for tracking significant changes in glacier terminus positions at the pixel level (Supplementary Figure 5).

The total area uncertainty was estimated with block bootstrapping [53]. The area estimator is:

$$A^* = a \cdot \sum_{i=1}^{n} p\left(T_i = 1\right) \,, \tag{2}$$

where a is the area of one pixel, n is the total number of pixels, and $p\left(T_i = 1\right)$ is the probability of the i^{th} pixel being a glacier defined as:

$$p\left(T_i = 1\right) = \begin{cases} C_i & \text{if } L_i = 1 \\ 1 - C_i & \text{else} \end{cases} \,, \tag{3}$$

with C_i and L_i being, respectively, the calibrated confidence and the model label assigned to the i^{th} pixel. We partitioned the entire archipelago into non-overlapping square windows of side length b (selected via the optimisation procedure described below). We then drew random resamples with replacement of these windows and calculated the corresponding area values, A^*. This process was repeated 10 000 times, and the corresponding area uncertainty bands were calculated as the 2.5^{th} and 97.5^{th} percentiles of the bootstrapping distribution of A^*.

The optimal window size b for block bootstrapping was estimated by minimising the mean squared error between bootstrapped distributions and known areas from the 2016/2017 [15] and 2020 [16] inventories:

$$\mathrm{E}\left[\left(A_b^* - A\right)^2\right] = \mathrm{Var}\left[A_b^*\right] + \left(\mathrm{E}\left[A_b^*\right] - A\right)^2 \to \min_b \,, \tag{4}$$

where A are the known total area values. We assumed insignificant total area change between 2016 and 2017, considering that only a single multi-year inventory covers both years and our results show a small area change between 2016 and 2017. Among three window sizes optimised independently for all three years, we chose the maximum one, noted for providing the highest variance, $b = 3.2$ km in 2020, resulting in a total sample of 5 330 windows. This window size was then applied to the remaining years for the final inference. Lastly, we recentred the bootstrapping distributions so their means match the vectorised outputs of the model, ensuring consistency between the reported figures and the generated inventories.

Kvitøya outlines. For completeness, we mapped Kvitøya from 2016 to 2024 using GlaViTU [27] and optical imagery, and published it together with the glacier inventories for the rest of the archipelago. We utilised Landsat 8 and 9 images that are suitable for glacier mapping, i.e. acquired close to the end of the ablation season with minimal cloud coverage and absence of sea ice. Successfully, we derived the outlines of Kvitøya for 2016, 2018, 2020, 2022, 2023 and 2024.

Accuracy assessment. The classification performance was evaluated using intersection over union (IoU), precision and recall, defined by:

$$\mathrm{IoU} = \left| T \cap P \right| / \left| T \cup P \right| \,, \tag{5}$$

$$\mathrm{Precision} = \left| T \cap P \right| / \left| P \right| \,, \tag{6}$$

$$\mathrm{Recall} = \left| T \cap P \right| / \left| T \right| \,, \tag{7}$$

where T and P denote the reference and predicted glacier pixels, respectively.

The differences in glacierised area were assessed using both absolute and relative metrics:

$$\Delta A = A_{\text{pred}} - A_{\text{ref}} \,, \quad \delta A = \left(A_{\text{pred}} - A_{\text{ref}}\right) / A_{\text{ref}} \,, \tag{8}$$

where A_{pred} is the predicted glacierised area, and A_{ref} is the reference area.

Distance deviations between the predicted and reference glacier boundaries were calculated using a PoLiS-like metric [54], which considers the average distances between boundary points:

$$\overline{\rho(\text{pred}, \text{ref})} = \frac{1}{\left|\{p \in \text{pred} \cup \text{ref}\}\right|} \left(\sum_{\{p \in \text{pred}\}} \rho\left(p, \text{ref}\right) + \sum_{\{p \in \text{ref}\}} \rho\left(p, \text{pred}\right) \right) , \tag{9}$$

where p stands for the boundary points, ref and pred are the reference and predicted boundaries, respectively, and ρ is the Euclidean distance. Points were sampled every 10 m along all boundaries within a tile to derive this metric. Additional statistics—median and the 95^{th} percentile—were provided to offer a more detailed view of the variation in distance deviations.

Computational resources. We trained and deployed the models on a cloud server equipped with an NVIDIA RTX A6000 GPU, a 128-core 2.5 GHz CPU and 1 TB RAM. The training duration for one model ranged from three to four days, depending on the number of input features. Applying the model to the complete dataset spanning 2016 to 2024 took a day.

Data availability

The datasets generated during and/or analysed during the current study will be available upon publication.

Code availability

Our codebase and the pretrained models will be available upon publication.

References

1. Hock, R. *et al.* High Mountain Areas. *IPCC Special Report on the Ocean and Cryosphere in a Changing Climate* (eds Pörtner, H.-O. *et al.*) 131–202. `https://www.ipcc.ch/srocc/chapter/chapter-2/` (2019).
2. Meredith, M. *et al.* Polar Regions. *IPCC Special Report on the Ocean and Cryosphere in a Changing Climate* (eds Pörtner, H.-O. *et al.*) 203–320. `https://www.ipcc.ch/srocc/chapter/chapter-3-2/` (2019).
3. Zemp, M. *et al.* Global glacier mass changes and their contributions to sea-level rise from 1961 to 2016. *Nature* **568,** 382–386. ISSN: 14764687 (7752 Apr. 2019).
4. Hugonnet, R. *et al.* Accelerated global glacier mass loss in the early twenty-first century. *Nature* **592,** 726–731. ISSN: 14764687 (7856 Apr. 2021).
5. Rounce, D. R. *et al.* Global glacier change in the 21st century: Every increase in temperature matters. *Science* **379,** 78–83. ISSN: 10959203. `https://www.science.org/doi/10.1126/science.abo1324` (6627 Jan. 2023).
6. Rantanen, M. *et al.* The Arctic has warmed nearly four times faster than the globe since 1979. *Nature Communications Earth & Environment* **3.** ISSN: 2662-4435. `https://www.nature.com/articles/s43247-022-00498-3` (1 Aug. 2022).

7. Osuch, M. & Wawrzyniak, T. Inter- and intra-annual changes in air temperature and precipitation in western Spitsbergen. *International Journal of Climatology* **37,** 3082–3097. eprint: https://rmets.onlinelibrary.wiley.com/doi/pdf/10.1002/joc.4901. https://rmets.onlinelibrary.wiley.com/doi/abs/10.1002/joc.4901 (2017).
8. Nuth, C. *et al.* Decadal changes from a multi-temporal glacier inventory of Svalbard. *The Cryosphere* **7,** 1603–1621. https://tc.copernicus.org/articles/7/1603/2013/ (2013).
9. Spolaor, A. *et al.* Climate change is rapidly deteriorating the climatic signal in Svalbard glaciers. *The Cryosphere* **18,** 307–320. https://tc.copernicus.org/articles/18/307/2024/ (2024).
10. Łupikasza, E. B. *et al.* The Role of Winter Rain in the Glacial System on Svalbard. *Water* **11.** ISSN: 2073-4441. https://www.mdpi.com/2073-4441/11/2/334 (2019).
11. Schuler, T. V. *et al.* Reconciling Svalbard Glacier Mass Balance. *Frontiers in Earth Science* **8.** ISSN: 2296-6463. https://www.frontiersin.org/journals/earth-science/articles/10.3389/feart.2020.00156 (2020).
12. Ingrosso, G. *et al.* Greening of Svalbard in the twentieth century driven by sea ice loss and glaciers retreat. *Communications Earth & Environment* **6,** 30. ISSN: 2662-4435. https://doi.org/10.1038/s43247-025-01994-y (Jan. 2025).
13. World Meteorological Organization, United Nations Environment Programme, International Science Council & Intergovernmental Oceanographic Commission of the United Nations Educational, Scientific and Cultural Organization. *The 2022 GCOS ECVs Requirements (GCOS 245)* 2022. https://library.wmo.int/idurl/4/58111.
14. Racoviteanu, A. E., Paul, F., Raup, B., Khalsa, S. J. S. & Armstrong, R. Challenges and recommendations in mapping of glacier parameters from space: results of the 2008 Global Land Ice Measurements from Space (GLIMS) workshop, Boulder, Colorado, USA. *Annals of Glaciology* **50,** 53–69. ISSN: 0260-3055 (53 2009).
15. Paul, F., Goerlich, F. & Rastner, P. *A new glacier inventory for Svalbard from Sentinel-2 and Landsat 8 for improved calculation of climate change impacts* in *EGU General Assembly* (2021, online, 19–30 Apr 2021, EGU21-14499). https://doi.org/10.5194/egusphere-egu21-14499.
16. Kohler, J., Lith, A. & Moholdt, G. *Svalbard glacier inventory based on Sentinel-2 imagery from summer 2020* 2021. https://doi.org/10.21334/npolar.2021.1b8631bf.
17. Muñoz-Hermosilla, J. M. *et al.* A 3D glacier dynamics–line plume model to estimate the frontal ablation of Hansbreen, Svalbard. *The Cryosphere* **18,** 1911–1924. https://tc.copernicus.org/articles/18/1911/2024/ (2024).
18. D. K. Atwood, F. M. & Arendt, A. Using L-band SAR coherence to delineate glacier extent. *Canadian Journal of Remote Sensing* **36,** S186–S195. eprint: https://doi.org/10.5589/m10-014. https://doi.org/10.5589/m10-014 (2010).
19. Lippl, S., Vijay, S. & Braun, M. Automatic delineation of debris-covered glaciers using InSAR coherence derived from X-, C- and L-band radar data: a case study of Yazgyl Glacier. *Journal of Glaciology* **64,** 811–821 (2018).
20. Hallikainen, M., Ulaby, F. & Abdelrazik, M. Dielectric properties of snow in the 3 to 37 GHz range. *IEEE Transactions on Antennas and Propagation* **34,** 1329–1340 (1986).
21. Winsvold, S. H. *et al.* Using SAR satellite data time series for regional glacier mapping. *The Cryosphere* **12,** 867–890. https://tc.copernicus.org/articles/12/867/2018/ (2018).
22. Barzycka, B., Błaszczyk, M., Grabiec, M. & Jania, J. Glacier facies of Vestfonna (Svalbard) based on SAR images and GPR measurements. *Remote Sensing of Environment* **221,** 373–385. ISSN: 0034-4257. https://www.sciencedirect.com/science/article/pii/S0034425718305297 (2019).
23. RGI Consortium. Randolph Glacier Inventory—A Dataset of Global Glacier Outlines, Version 7. *Boulder, Colorado USA. NSIDC: National Snow and Ice Data Center.* (2023).
24. Nuth, C. *et al.* Dynamic vulnerability revealed in the collapse of an Arctic tidewater glacier. *Scientific Reports* **9,** 5541. ISSN: 2045-2322. https://doi.org/10.1038/s41598-019-41117-0 (Apr. 2019).
25. Dunse, T. *et al.* Glacier-surge mechanisms promoted by a hydro-thermodynamic feedback to summer melt. *The Cryosphere* **9,** 197–215. https://tc.copernicus.org/articles/9/197/2015/ (2015).
26. Strozzi, T., Cantus, O. & Santoro, M. *Glaciers_CCI project: ERS-1/2 C-band data over Svalbard* Project Report (GAMMA Remote Sensing AG, Switzerland, Oct. 2024).
27. Maslov, K. A., Persello, C., Schellenberger, T. & Stein, A. Globally scalable glacier mapping by deep learning matches expert delineation accuracy. *Nature Communications* **16,** 43. ISSN: 2041-1723. https://doi.org/10.1038/s41467-024-54956-x (2025).
28. Van Pelt, W. *et al.* A long-term dataset of climatic mass balance, snow conditions, and runoff in Svalbard (1957–2018). *The Cryosphere* **13,** 2259–2280. https://tc.copernicus.org/articles/13/2259/2019/ (2019).
29. Paul, F. *et al.* On the accuracy of glacier outlines derived from remote-sensing data. *Annals of Glaciology* **54,** 171–182. ISSN: 02603055 (July 2013).
30. Raup, B. H. *et al.* Quality in the GLIMS Glacier Database. *Global Land Ice Measurements from Space,* 163–182. https://link.springer.com/chapter/10.1007/978-3-540-79818-7_7 (2014).
31. Linsbauer, A. *et al.* The New Swiss Glacier Inventory SGI2016: From a Topographical to a Glaciological Dataset. *Frontiers in Earth Science* **9,** 704189. ISSN: 22966463 (Oct. 2021).
32. Geyman, E., van Pelt, W., Maloof, A., Aas, H. & Kohler, J. *1936/1938 DEM of Svalbard* 2021. https://doi.org/10.21334/npolar.2021.f6afca5c.
33. Geyman, E. C., J. J. van Pelt, W., Maloof, A. C., Aas, H. F. & Kohler, J. Historical glacier change on Svalbard predicts doubling of mass loss by 2100. *Nature* **601,** 374–379. ISSN: 1476-4687. https://doi.org/10.1038/s41586-021-04314-4 (Jan. 2022).

34. Zekollari, H., Huss, M. & Farinotti, D. On the Imbalance and Response Time of Glaciers in the European Alps. *Geophysical Research Letters* **47.** e2019GL085578 2019GL085578, e2019GL085578. eprint: https://agupubs.onlinelibrary.wiley.com/doi/pdf/10.1029/2019GL085578. https://agupubs.onlinelibrary.wiley.com/doi/abs/10.1029/2019GL085578 (2020).

35. Urbański, J. A. & Litwicka, D. The decline of Svalbard land-fast sea ice extent as a result of climate change. *Oceanologia* **64,** 535–545. ISSN: 0078-3234. https://www.sciencedirect.com/science/article/pii/S0078323422000495 (2022).

36. Krug, J., Durand, G., Gagliardini, O. & Weiss, J. Modelling the impact of submarine frontal melting and ice mélange on glacier dynamics. *The Cryosphere* **9,** 989–1003. https://tc.copernicus.org/articles/9/989/2015/ (2015).

37. Morris, A., Moholdt, G. & Gray, L. Spread of Svalbard Glacier Mass Loss to Barents Sea Margins Revealed by CryoSat-2. *Journal of Geophysical Research: Earth Surface* **125.** e2019JF005357 10.1029/2019JF005357, e2019JF005357. eprint: https://agupubs.onlinelibrary.wiley.com/doi/pdf/10.1029/2019JF005357. https://agupubs.onlinelibrary.wiley.com/doi/abs/10.1029/2019JF005357 (2020).

38. Tepes, P. *et al.* Changes in elevation and mass of Arctic glaciers and ice caps, 2010–2017. *Remote Sensing of Environment* **261,** 112481. ISSN: 0034-4257. https://www.sciencedirect.com/science/article/pii/S0034425721001991 (2021).

39. Li, T. *et al.* Pervasive glacier retreats across Svalbard from 1985 to 2023. *Nature Communications* **16,** 705. ISSN: 2041-1723. https://doi.org/10.1038/s41467-025-55948-1 (Jan. 2025).

40. Wood, M. *et al.* Ocean-Induced Melt Triggers Glacier Retreat in Northwest Greenland. *Geophysical Research Letters* **45,** 8334–8342. eprint: https://agupubs.onlinelibrary.wiley.com/doi/pdf/10.1029/2018GL078024. https://agupubs.onlinelibrary.wiley.com/doi/abs/10.1029/2018GL078024 (2018).

41. Leclercq, P. W., Kääb, A. & Altena, B. Brief communication: Detection of glacier surge activity using cloud computing of Sentinel-1 radar data. *The Cryosphere* **15,** 4901–4907. https://tc.copernicus.org/articles/15/4901/2021/ (2021).

42. Beraud, L., Brun, F., Dehecq, A., Hugonnet, R. & Shekhar, P. Glacier surge monitoring from temporally dense elevation time series: application to an ASTER dataset over the Karakoram region. *EGUsphere* **2024,** 1–32. https://egusphere.copernicus.org/preprints/2024/egusphere-2024-3480/ (2024).

43. Guillet, G. *et al.* A regionally resolved inventory of High Mountain Asia surge-type glaciers, derived from a multi-factor remote sensing approach. *The Cryosphere* **16,** 603–623. https://tc.copernicus.org/articles/16/603/2022/ (2022).

44. Frey, O., Santoro, M., Werner, C. L. & Wegmuller, U. DEM-Based SAR Pixel-Area Estimation for Enhanced Geocoding Refinement and Radiometric Normalization. *IEEE Geoscience and Remote Sensing Letters* **10,** 48–52 (2013).

45. Maslov, K. A., Schellenberger, T., Persello, C. & Stein, A. *Glacier Mapping from Sentinel-1 SAR Time Series with Deep Learning in Svalbard* in *IGARSS 2024 - 2024 IEEE International Geoscience and Remote Sensing Symposium* (2024), 14–17.

46. Ronneberger, O., Fischer, P. & Brox, T. U-Net: Convolutional Networks for Biomedical Image Segmentation. *Lecture Notes in Computer Science (including subseries Lecture Notes in Artificial Intelligence and Lecture Notes in Bioinformatics)* **9351,** 234–241. ISSN: 16113349. https://arxiv.org/abs/1505.04597v1 (May 2015).

47. Tran, D., Bourdev, L., Fergus, R., Torresani, L. & Paluri, M. *Learning Spatiotemporal Features With 3D Convolutional Networks* in *Proceedings of the IEEE International Conference on Computer Vision (ICCV)* (Dec. 2015).

48. Kingma, D. P. & Ba, J. L. *Adam: A Method for Stochastic Optimization* in *3rd International Conference on Learning Representations, ICLR 2015 - Conference Track Proceedings* (International Conference on Learning Representations, ICLR, Dec. 2014). https://arxiv.org/abs/1412.6980v9.

49. Lin, T.-Y., Goyal, P., Girshick, R., He, K. & Dollár, P. *Focal Loss for Dense Object Detection* in *2017 IEEE International Conference on Computer Vision (ICCV)* (2017), 2999–3007.

50. Müller, R., Kornblith, S. & Hinton, G. When Does Label Smoothing Help? *Advances in Neural Information Processing Systems* **32.** ISSN: 10495258. https://arxiv.org/abs/1906.02629v3 (June 2019).

51. Loshchilov, I. & Hutter, F. *SGDR: Stochastic Gradient Descent with Warm Restarts* in *5th International Conference on Learning Representations, ICLR 2017 - Conference Track Proceedings* (International Conference on Learning Representations, ICLR, Aug. 2016). https://arxiv.org/abs/1608.03983v5.

52. Paul, F. *et al.* Recommendations for the compilation of glacier inventory data from digital sources. *Annals of Glaciology* **50,** 119–126. ISSN: 0260-3055. https://www.cambridge.org/core/journals/annals-of-glaciology/article/recommendations-for-the-compilation-of-glacier-inventory-data-from-digital-sources/6BAE48BE4B8FEEEEBCFB59A2684A2427 (53 2009).

53. Hall, P., Horowitz, J. L. & Jing, B.-Y. On Blocking Rules for the Bootstrap with Dependent Data. *Biometrika* **82,** 561–574. ISSN: 00063444, 14643510. http://www.jstor.org/stable/2337534 (1995).

54. Avbelj, J., Müller, R. & Bamler, R. A Metric for Polygon Comparison and Building Extraction Evaluation. *IEEE Geoscience and Remote Sensing Letters* **12,** 170–174 (2015).

Acknowledgements

This research was financed by the Research Council of Norway under the "Researcher Project for Scientific Renewal" (project MASSIVE, no. 315971) awarded to T.S., C.P., A.S. and K.A.M. Additional support was provided by Open Clouds for Research Environments under the EU H2020 programme (project MATS_CLOUD, no. 824079) for access to the CREODIAS cloud platform for computing and seamless remote sensing data retrieval, awarded to C.P., T.S. and K.A.M.

We thank J. Kohler, A. Lith and G. Moholdt from the Norwegian Polar Institute for generously providing an early version of the 2020 Svalbard inventory used for model training and T. Strozzi from GAMMA Remote Sensing AG for generously providing the glacier surge inventory for Svalbard. We also kindly thank E. S. Mannerfelt from the University of Oslo for providing us with the updated dynamic basin boundaries of Austfonna, Basin-3 (Supplementary information).

Author contributions

T.S., K.A.M. and C.P. designed the study. K.A.M. implemented the methods and conducted the analysis. K.A.M., T.S., C.P. and A.S. discussed the results extensively. T.S. had the project idea and leads the project with C.P. K.A.M. wrote the manuscript. T.S., C.P. and A.S. reviewed the manuscript.

Competing interests

The authors declare no competing interests.

Supplementary information

Three times accelerated glacier area loss in Svalbard revealed by deep learning

Konstantin A. Maslov, Thomas Schellenberger, Claudio Persello, Alfred Stein

Supplementary Notes

Austfonna, Basin-7 surge. In our analysis for the 2016–2024 epoch, a notable positive anomaly was observed in the area change of Austfonna's Basin-7. Upon detailed examination, we believe this anomaly indicates a surge event previously unreported in the most comprehensive surge inventory known to us [1]. This event started in 2019, with the glacier front advancing by approximately 1.2 km over two years.

The hypothesis of a surge is further supported by changes in radar backscatter observed in the time series of SAR imagery, as shown in Supplementary Figure 1. Increased backscatter is typically linked with increased crevassing, which is a common feature of surging glaciers [2, 3].

Interestingly, while the velocity anomaly characteristic of this surge was detected by the authors of the inventory [1], it was not included in their final publication. Based on the observations of area change and SAR data time series, we advocate for the inclusion of this event in updated surge inventories. We argue that these indicators clearly point to active surging behavior, which should not be overlooked.

This finding showcases the utility of annually updated glacier inventories, not as a superior method, but as a valuable complementary tool that can enhance more traditional methods for surge detection.

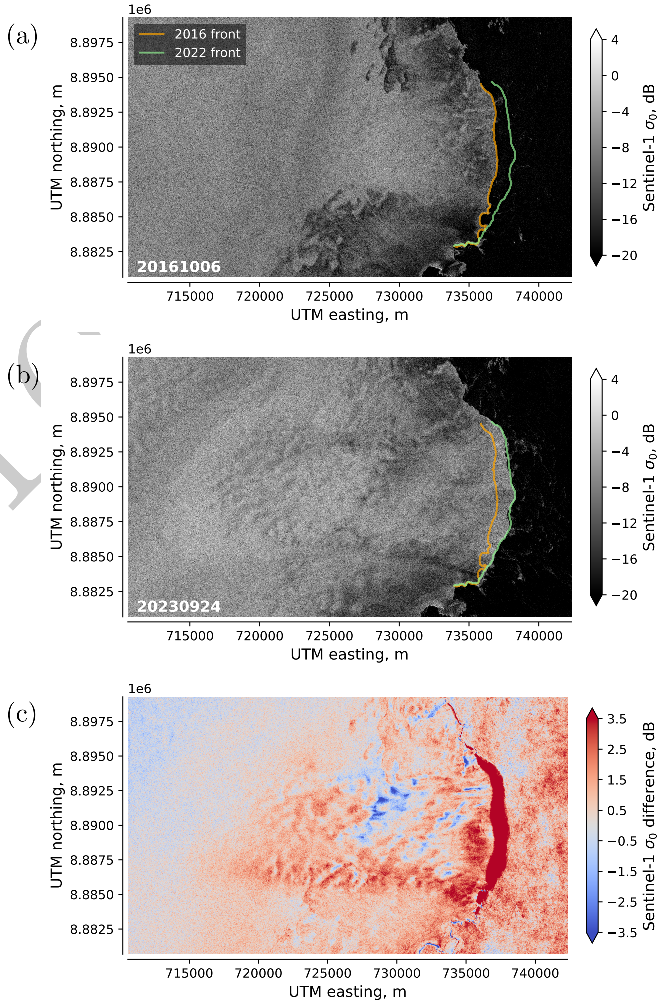

Supplementary Fig. 1 Glacier surge of Austfonna, Basin-7: **a** a Sentinel-1 image from Autumn 2016, **b** an image from Autumn 2023 and **c** backscatter difference of two averaged images from 2019–2022 and 2016–2018. An animated version is available at `https://figshare.com/s/caf969067065a0d968ae`. Copernicus Sentinel data 2016–2025.

Supplementary Figures and Tables

Supplementary Table 1 Validation performance of ICEmapper in different training settings.

Feature set	Pooling	IoU[a]	
		Patch-wise	Pixel-wise
GRD	max	0.875	0.960
GRD	time-weighted	0.877	0.962
RTC	time-weighted	0.883	0.962
InSAR	time-weighted	0.847	0.939
GRD+InSAR	time-weighted	**0.89346**	**0.963**
RTC+InSAR	time-weighted	0.89323	0.962

[a] The best IoU values are in bold.

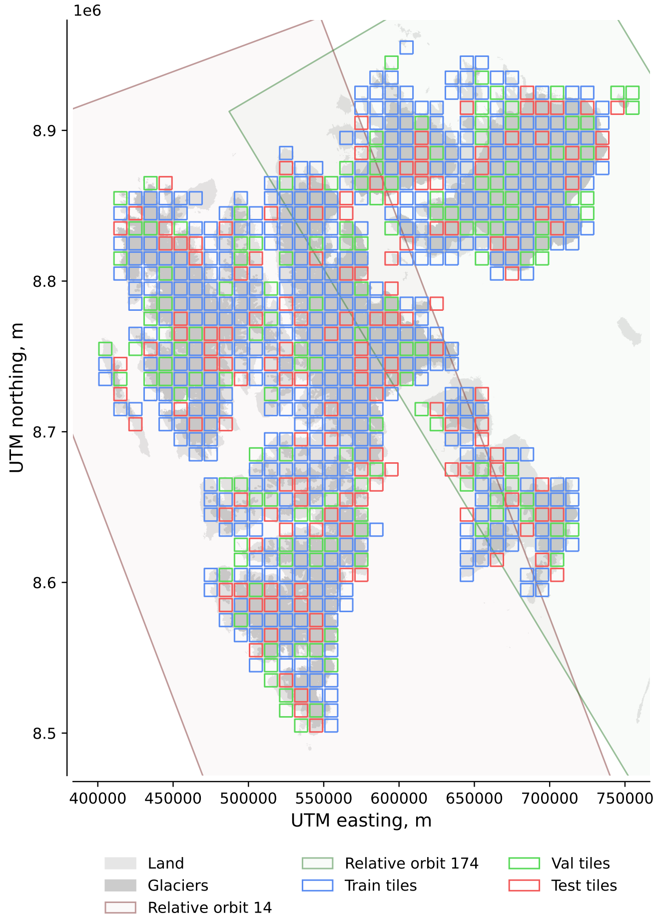

Supplementary Fig. 3 Study area overview. Tile sizes are reduced for visualisation purposes. The glacier outlines are taken from Kohler et al., 2021 [5].

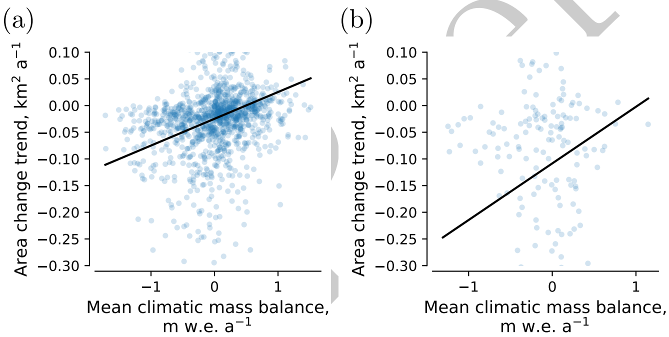

Supplementary Fig. 2 Glacier area change rate against climatic mass balance [4]: a for land-terminating (r_s = 0.32, p-value < 0.05) and **b** for tidewater ($r_s = 0.13$, p-value > 0.05) glaciers in the RGI7.0–2016 epoch averaged per glacier.

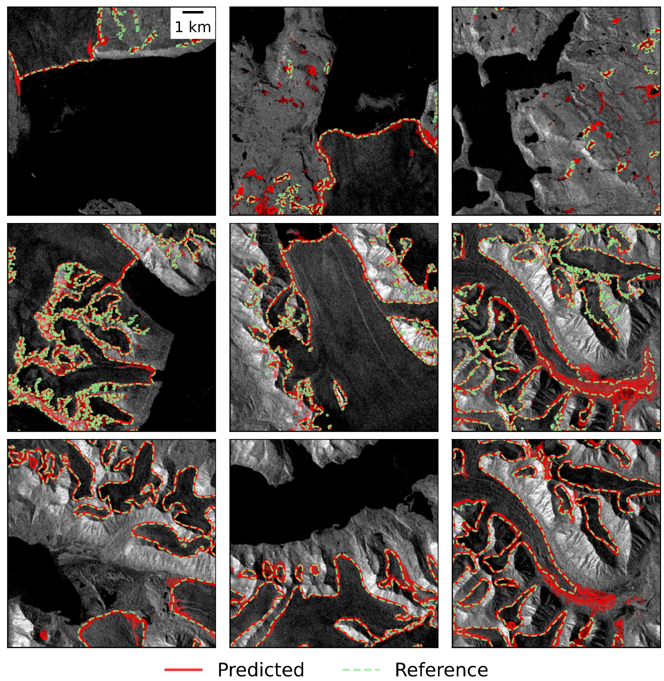

Supplementary Fig. 4 Closeups of test classification results. The 95%-confidence bands are shown as red transparent areas. Copernicus Sentinel data 2016, 2017 and 2020.

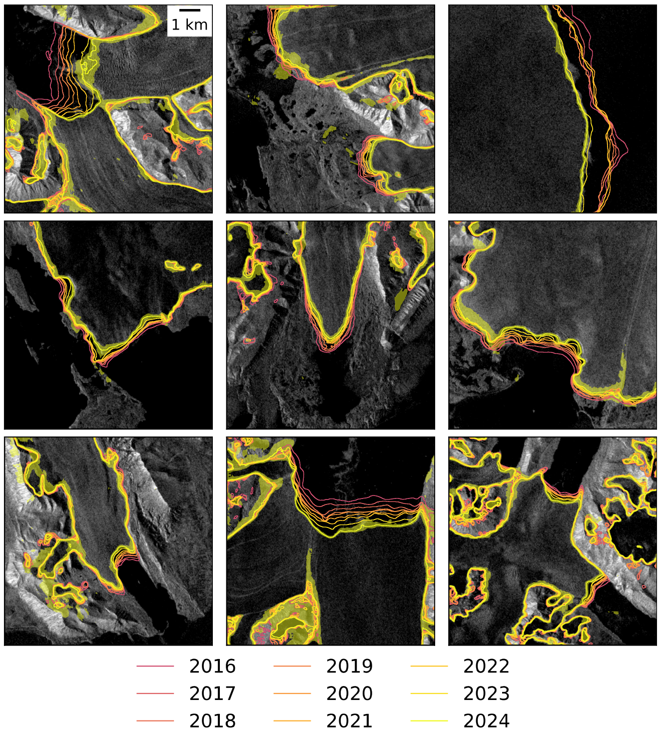

Supplementary Fig. 5 Significant changes in glacier outlines found at the pixel level. The 95%-confidence bands are shown as yellow transparent areas. For clarity, confidence bands are presented only for 2024. Copernicus Sentinel data 2024.

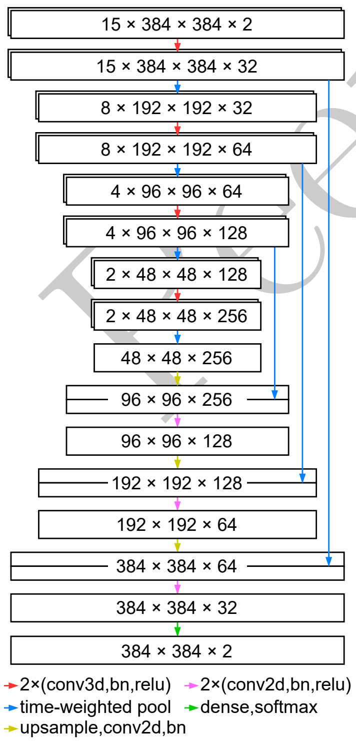

Supplementary Fig. 6 Intensity-Coherence-Evolution-mapper (ICEmapper). Boxes and numbers in them represent tensors and their shapes in the [time×]height × width × channels format, and arrows indicate operations.

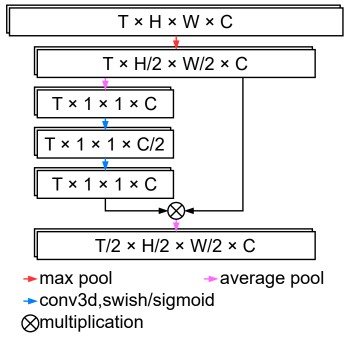

Supplementary Fig. 7 Time-weighted pooling block. Text in boxes represents tensor shapes in the time × height × width × channels format, and arrows indicate operations and data flow.

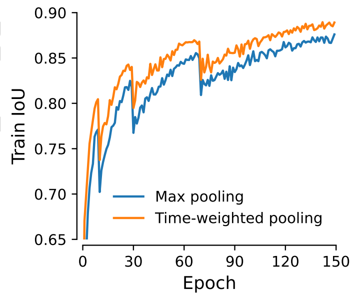

Supplementary Fig. 8 Train IoU dynamics for ICEmapper trained with GRD only data with max pooling and time-weighted pooling.

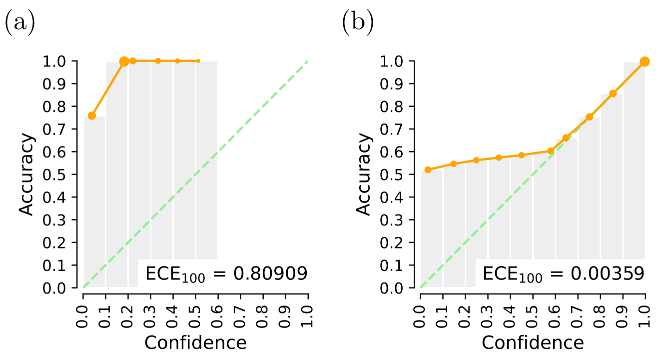

Supplementary Fig. 9 Reliability diagrams: a before and **b** after confidence calibration. ECE stands for expected calibration error. Green lines indicate the ideal calibration case. The marker sizes are proportional to the number of pixels within a bin.

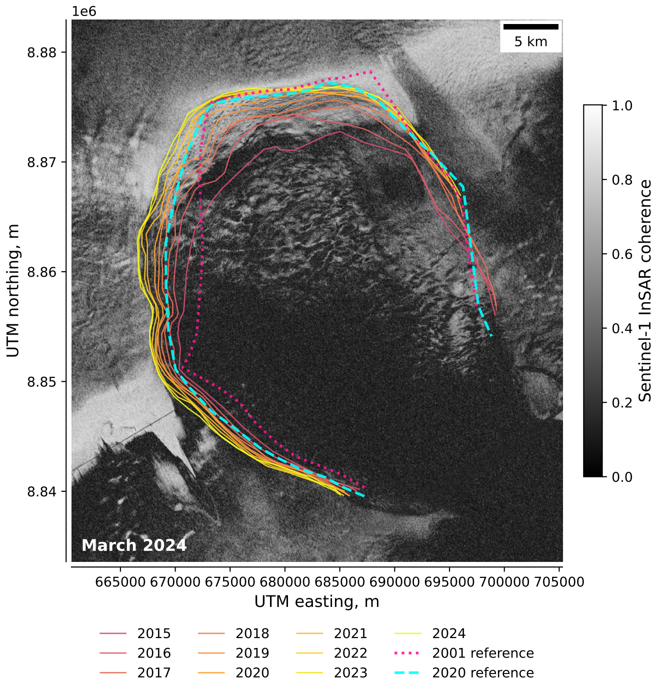

Supplementary Fig. 10 Surge-induced expansion of Austfonna, Basin-3 dynamic extent observed in InSAR coherence images. The 2020 reference ice divides are from Kohler et al., 2021 [5], and the 2001 reference ice divides are from RGI7.0 [6]. Copernicus Sentinel data 2024.

References

1. Strozzi, T., Cantus, O. & Santoro, M. *Glaciers_CCI project: ERS-1/2 C-band data over Svalbard* Project Report (GAMMA Remote Sensing AG, Switzerland, Oct. 2024).

2. Leclercq, P. W., Kääb, A. & Altena, B. Brief communication: Detection of glacier surge activity using cloud computing of Sentinel-1 radar data. *The Cryosphere* **15,** 4901–4907. `https://tc.copernicus.org/articles/15/4901/2021/` (2021).

3. Kääb, A., Bazilova, V., Leclercq, P. W., Mannerfelt, E. S. & Strozzi, T. Global clustering of recent glacier surges from radar backscatter data, 2017–2022. *Journal of Glaciology* **69,** 1515–1523 (2023).

4. Van Pelt, W. *et al.* A long-term dataset of climatic mass balance, snow conditions, and runoff in Svalbard (1957–2018). *The Cryosphere* **13,** 2259–2280. `https://tc.copernicus.org/articles/13/2259/2019/` (2019).

5. Kohler, J., Lith, A. & Moholdt, G. *Svalbard glacier inventory based on Sentinel-2 imagery from summer 2020* 2021. `https://doi.org/10.21334/npolar.2021.1b8631bf`.

6. RGI Consortium. Randolph Glacier Inventory—A Dataset of Global Glacier Outlines, Version 7. *Boulder, Colorado USA. NSIDC: National Snow and Ice Data Center.* (2023).